

Corrosion-resistant and high-entropic non-noble metal bifunctional electrodes for PEM-type water electrolyser

Aimi Tajuddin

University of Tsukuba

Mitsuru Wakisaka

Toyama Prefectural University

Tatsuhiko Ohto

Graduate School of Engineering Science, Osaka University <https://orcid.org/0000-0001-8681-3800>

Yue Yu

University of Tsukuba

Haruki Fukushima

Toyama Prefectural University

Hisanori Tanimoto

University of Tsukuba

Ganesan Elumalai

University of Tsukuba

Yoshitatsu Misu

JX Nippon Oil & Energy Corporation

Samuel Jeong

University of Tsukuba

Jun-ichi Fujita

University of Tsukuba

Hirokazu Tada

Osaka University

Takeshi Fujita

Kochi University of Technology <https://orcid.org/0000-0002-2318-0433>

Kaori Takano

JX Nippon Oil & Energy Corporation <https://orcid.org/0000-0001-7963-9664>

Koji Matsuoka

JX Nippon Oil & Energy Corporation

Yasushi Sato

JX Nippon Oil & Energy Corporation

Yoshikazu Ito (✉ ito.yoshikazu.ga@u.tsukuba.ac.jp)

Article

Keywords:

Posted Date: March 10th, 2022

DOI: <https://doi.org/10.21203/rs.3.rs-1345467/v1>

License:   This work is licensed under a Creative Commons Attribution 4.0 International License.

[Read Full License](#)

Abstract

To realise sustainable hydrogen economy, corrosion-resistant non-noble metal catalysts are needed to replace catalysts based on noble metals. The combination of passivation elements and catalytically active elements is crucial for simultaneously achieving high corrosion resistance and high catalytic activity. Here, we investigated the self-selection/reconstruction characteristics of multi-element (nonary) alloys that could automatically redistribute suitable elements and rearrange surface structures under the target reaction conditions. We found the following synergetic effect (i.e. cocktail effect) among the elements: Ti, Zr, Nb, and Mo significantly contribute to passivation, whereas Cr, Co, Ni, Mn, and Fe enhance the catalytic activity. Practical water electrolysis experiments showed that the self-selected/reconstructed multi-element alloy demonstrates high performance in proton exchange membrane (PEM)-type water electrolysis without obvious degeneration during stability tests, verifying the alloy's resistance to corrosion in a practical PEM electrolyser.

Introduction

Hydrogen (H_2) is important for achieving carbon neutrality, both as a next-generation energy source and an energy carrier when combined with fuel cells. Water electrolysis driven by renewable energy is a promising technology¹⁻³ for hydrogen production with zero emission. Water electrolysis can be classified into the alkaline type⁴, proton exchange membrane (PEM) type^{5,6}, and anion exchange membrane (AEM) type^{7,8}. Compared to the other types, PEM-type water electrolysis is considered eco-friendly and efficient because it generates no waste, produces very pure H_2 gas (> 99.9999 vol% for PEM-type vs. >99.5 vol% for alkaline type and > 99.99 vol% for AEM-type)⁹, and displays a high discharge H_2 pressure (30–76 bar)¹⁰ and a high current density ($1.0 - 4.0 \text{ A cm}^{-2}$) at low overpotentials ($1.5 - 1.9 \text{ V}$)^{3,6,10,11}. However, efficient electrocatalytic reactions in these systems require considerable amounts of noble metals, for example, 300 kg of Pt in the cathode and 700 kg of Ir in the anode per 1.0 GW of power input of electrolyser¹¹. The scarcity of noble metals, especially that of Ir (global production: 63 kt/year)¹¹, makes it difficult for PEM-type water electrolysis to reach net-zero carbon and sustainable development goals (SDGs). Unfortunately, researchers have made little progress toward finding alternative electrode materials for PEM-type electrolysers, i.e. the reaction environment (ex. severe oxidation conditions under a high operation voltage) wherein even noble metals can be dissolved ($1.5 \text{ ng cm}^{-2} \text{ h}^{-1}$ dissolution rate for Pt and $0.1 \text{ ng cm}^{-2} \text{ h}^{-1}$ dissolution rate for Ir)^{12,13}. Thus, a key challenge is to develop highly corrosion-resistant non-noble metal electrodes with the performance comparable to noble metal electrodes.

Multi-element alloys containing five or even more metals, called high entropy alloy, is a promising candidate to replace noble metals. Some non-noble metal high entropy alloys displayed excellent catalytic ability in half-cell reactions (i.e. hydrogen evolution reaction (HER) and oxygen evolution reaction (OER)) in alkaline or acidic electrolytes¹⁴⁻²². In addition, their corrosion is suppressed through passivation (i.e., forming metal hydroxides or oxides) and the corrosion characteristics resemble those of Cu-based alloys in seawater²³. However, there has been no systematic investigation of their corrosion

resistance mechanisms, or the functions and synergy (i.e. cocktail effect) of each element in the high entropy alloy catalysts with combining both in situ-type electrochemical experiments and theoretical calculations. The reason is that large number of combinations of elements and their compositions, as well as the resulting system complexity, impedes the rational design, optimisation and computational simulation of high entropy alloys. Moreover, no full-cell experiments using PEM-type water electrolyser have been successfully carried out to verify that noble metal-based electrodes can be replaced by those completely free from noble metals.

In this study, we propose a new approach to design high-entropic alloys (abbreviated to HEAs) from the viewpoints of self-selection of elements and self-reconstruction of structures in target reaction conditions (Scheme 1). The conventional exploration of HEAs adopts a bottom-up approach, in which different numbers and combinations of metal species are systematically investigated for optimisation by adding one element at a time. In contrast, in our top-down approach, first HEAs are prepared with a sufficient number of elements, and the composition in its surface structure is automatically selected in the target reaction conditions and subsequently rearranged under an applied voltage. This 'self-selection', namely the dealloying of easy-to-dissolve metals, produces surface structures similar to those in an HEA consisting of only passivation elements and the surface structure after the 'self-reconstruction' helps us elucidate the catalytic reaction on the 'selected' surface. Thus, we can focus the combination of initial elements and the performance evaluation, bypassing the lengthy trial-and-error process that is necessary in the bottom-up approach. Using this concept, we investigate the effects of applied potential on the corrosion behaviours of a nonary non-noble metal alloy (Ti, Cr, Mn, Fe, Co, Ni, Zr, Nb, and Mo) by quasi in-situ electrochemical X-ray photoelectron spectroscopy (EC-XPS)^{24,25} under similar conditions of PEM-type electrolysis. We identify an origin of the synergetic effect in the nonary alloy. (1) EC-XPS reveals that Ti, Zr, Nb, and Mo significantly contribute to passivation, while Cr, Ni, and Co are involved in redox processes during the potential cycles. (2) Density functional theory (DFT) calculation reveals that Cr, Co, Ni, Mn, and Fe enhance the catalytic activity. These conclusions are verified by comparing the performances of the nonary, quaternary (Ti, Zr, Nb, and Mo), and quinary (Cr, Mn, Fe, Co, and Ni) alloys in a practical PEM-type electrolyser. The nonary alloy catalysts achieved high bifunctional catalytic activity as anodes and cathodes with long lifetimes. This study provides new candidates and insights for replacing noble metals with non-noble metals for not only PEM-type water electrolysers but also other water electrolysers, fuel cells, and electrolytic synthesis cells for electrochemical CO₂ reduction.

Results

Synthesis and characterisation of HEAs

Quaternary, quinary, and nonary alloys were synthesised by conventional arc melting. Mother metal ingots were melted uniformly to obtain a 20-g button ingot of quaternary (Nb, Zr, Mo, and Ti; denoted as 4eHEA), quinary (Cr, Mn, Fe, Co, and Ni; denoted as 5eHEA), or nonary (Ti, Cr, Mn, Fe, Co, Ni, Zr, Nb, and Mo; denoted as 9eHEA) alloy (**Fig. 1a**). The crystal structures suggest that 9eHEA contains new phases unlike those seen in 4eHEA and 5eHEA (**Fig. 1b**). X-ray fluorescence (XRF) spectroscopy results show that

all HEAs contained different metals at almost the same molar ratios (**Supplementary Table 1**). The button ingot was mechanically crushed by ball milling to reach a particle size of 500–1000 nm (**Supplementary Fig. S1**). The specific surface areas measured by nitrogen adsorption/desorption method based on the Brunauer–Emmett–Teller (BET) theory²⁶ are 43.1, 2.7, and 4.7 m²g⁻¹ for 4eHEA, 5eHEA, and 9eHEA, respectively (**Supplementary Fig. S2**). Dark-field scanning transmission electron microscopy (DF-STEM) was used to examine the mechanically crushed 9eHEA particles (**Fig. 1c**). The high-resolution DF-STEM image revealed an amorphous-like lattice with high and low intensity distributions at the atomic scale (**Fig. 1d** and **Supplementary Fig. S3**), indicating an absence of obvious segregation in any of the elements. In addition, the elemental maps indicate that the nine elements were uniformly distributed in the alloys, and therefore there was no obvious phase separation at the atomic scale on the crushed particles. We further investigated the chemical binding states of HEAs after ball milling through X-ray photoelectron spectroscopy (XPS). XPS can detect metallic states of elements in HEA with partial oxidation under air conditions (**Supplementary Figs. S4–S7**). For electrochemical tests, the milled HEAs were mixed with commercially available carbon black (CB) as dispersing supports (**Supplementary Figs. S2** and **S8**).

Corrosion behaviours of HEAs

The corrosion behaviours of the HEAs were studied in a N₂-saturated 0.5 M aqueous H₂SO₄ electrolyte at 25 °C (**Fig. 2a** and **Supplementary Fig. S9**). The anodic polarisation curve from -0.55 to 2.2 V (vs. reversible hydrogen electrode (RHE)) and the cathodic polarisation curve from 2.2 to -0.55 V (vs. RHE) for the HEAs demonstrate a single cross potential (E_{cor}). From the anodic polarisation curves of 9eHEA, the corrosion current density (i_{cor}) at E_{cor} was estimated²⁷ as 1.26 $\mu\text{A cm}^{-2}$ at 0.11 V. This E_{cor} value is close to that of bulk Cu (0.22 V)²⁸. The i_{cor} value is higher than that of bulk Pt²⁹, but lower than those of Pt nanoparticles³⁰, Pt-based alloy nanoparticles³¹, bulk non-noble metals (Ni, Cu, and Fe)^{28,32,33}, 304 stainless steel³⁴, Ni phosphide alloys³², high entropy alloys^{34–36}, 4eHEA, and 5eHEA at similar conditions (**Fig. 2b** and **Supplementary Table 2**). Moreover, the polarisation curves of 9eHEA at 2.20 V (vs. RHE) reveal no obvious hysteresis (**Supplementary Fig. S9**), which indicates that this HEA has high corrosion resistance without pitting-type corrosion³⁷.

EC-XPS measurements of 9eHEA

The surface states and corrosion behaviours of 9eHEA were further investigated by EC-XPS in an N₂-saturated 2.5 mM aqueous H₂SO₄ electrolyte (**Figs. 2c–f**, **Supplementary Figs. S7** and **S10**, and **Supplementary Tables 3** and **4**). The linear sweep voltammograms were obtained from 0.14 (open circuit potential, (OCP)) to -0.30 V for HER processes and from 0.14 (OCP) to 1.9 V for OER processes. There were no significant differences in the EC-XPS data between the OCP and HER state, indicating that the metallic state of HEA was preserved during the reduction processes (**Figs. 2d–f**). In the OER processes at OCP, metallic Ti, Cr, Zr, Nb, and Mo were partially oxidised to TiO₂, Cr(OH)₃, ZrO₂, Nb₂O₅, and MoO₂ as oxide layers, respectively. Mn, Fe, Co, and Ni were mostly maintained despite some partial

dissolution. At the 1st oxidation stage (0.92 V), Ti, Cr, Mn, Zr, and Nb were further oxidised. Mo was oxidised to MoO₂ and MoO₃. Mn, Fe, Co, and Ni were partially oxidised to Mn₂O₃, Fe₂O₃/Fe₃O₄, Co(OH)₂, and Ni(OH)₂, respectively. At the 2nd oxidation stage (1.65 V), Cr, Co, and Ni showed potential-dependent oxidation, which turned Cr(OH)₃, Co(OH)₂, and Ni(OH)₂ to CrO₃, CoO/CoO₂, and NiO/NiO₂, respectively. At the OER stage (1.90 V), all elements on the surface were completely oxidised. After OER, the OCP was negatively shifted to 0.89 V, and so the OER process was irreversible. This could be attributed to metal leaching from 9eHEA during the OER processes and the redox reactions of Cr, Co, and Ni. Note that the shift in binding energy of Ti, Zr, Nb, and Mo is proportional to the applied potential between OCP and 1.90 V (**Supplementary Fig. S10**), which indicates that their chemical states (i.e. oxidised state) are potential-independent. Hence, their oxides work as passivation layers. These results during the OER processes suggest that the nine metals play three different roles: (i) passivation (Ti, Zr, Nb, and Mo), (ii) redox-active (Co, Ni, and Cr), and (iii) others (Mn and Fe).

Depth analysis of each element was carried out using angle-resolved EC-XPS (**Supplementary Figs. S7 and S11 and Supplementary Table S4**). XPS data at the HER stage are similar to that at OCP, indicating that all elements had identical distribution. In contrast, XPS data at the OER stage indicate that Ti, Cr, Mn, Fe, Zr, Nb, and Mo were distributed uniformly along the depth direction, while Co and Ni showed angle-dependent distributions. Considering the higher concentrations of Co and Ni atoms on the surface at 1.90 V than at other potentials, these two elements were segregated only at the OER stage due to the place exchange^{38,39} with oxygen species (**Scheme 1**). After the OER stage, Co and Ni penetrated the underlying passivation layers. Thus, the OER activity was enhanced by the self-reconstruction of Co and Ni (i.e., segregation on the surface) that only occurs during the OER stage.

PEM-type water electrolysis

After confirming the high corrosion resistance of our HEAs, we employed them as anode or cathode catalysts in a membrane-electrode assembly (MEA) to verify the feasibility of a single-cell (4.0 cm²) PEM-type electrolyser (**Supplementary Fig. S12**). To understand the catalytic activity of each HEA on individual electrodes, we prepared three types of MEAs (**Supplementary Fig. S13**): commercially available Pt/C cathode catalyst + HEA anode catalyst (abbreviated as Pt/C-HEA), HEA cathode catalyst + commercially available IrO₂ anode catalyst (abbreviated as HEA-IrO₂), as well as Pt/C cathode catalyst + IrO₂ anode catalyst (abbreviated as Pt/C-IrO₂) for benchmarking. Before the test, we optimised the ball-milling conditions and the catalyst loading (**Supplementary Fig. S14**). To fairly compare the catalytic activity of different HEAs, the *I*-*V* curves obtained using 4eHEA, 5eHEA, and 9eHEA as anode and cathode catalysts were normalised by the respective BET surface area of HEAs (**Figs. 3a–3b and Supplementary Fig. S15**). When HEA was used as cathode or anode, 9eHEA-IrO₂ and Pt/C-9eHEA showed higher performances than those using 4eHEA or 5eHEA. The cell voltage of 9eHEA at 1.0 A cm⁻² current density normalised by the electrode surface area (4.0 cm²) show 0.30 V (cathode) and 0.56 V (anode) higher than that of Pt/C-IrO₂

(1.58 V) (**Fig. 3c**). Their performances are comparable with reported noble metal catalysts and noble/non-noble alloy metal catalysts in the PEM electrolyser (**Supplementary Table S5**). The 1.88 V (78.7%) and 2.14 V (69.2%) cell voltages of 9eHEA at 1.0 A cm^{-2} bring 15.0% and 24.5% energy conversion efficiency loss of the electrolyser⁷ in comparison to the Pt/C-IrO₂ case (93.7%). Moreover, from the electrical impedance data, their Ohmic resistance and charge transfer resistance are close to those of Pt/C-IrO₂ (**Supplementary Fig. S16**).

Next, the cycling stability and durability of HEA catalysts were investigated (**Figs. 3c and 3d**). After 1,000 cycles, Pt/C-9eHEA showed no degradation at 5.0 A cm^{-2} , while 9eHEA-IrO₂ showed 5.4% reduction. Chronoamperometry (CP) tests of 9eHEA at a current density of 1.0 A cm^{-2} for 100 h resulted in a current density reduction of 13% (cathode) and 0% (anode). After the CP test, the morphology and chemical state of catalysts on the MEA were investigated. Cross-sectional SEM images of MEA and XRD spectra demonstrate that the original microstructures were well preserved (**Supplementary Figs. S17 and S18**). DF-STEM and elemental mapping of 9eHEA anode catalysts revealed a homogeneous distribution without obvious pitting corrosion (**Supplementary Fig. S19**). XPS data of 9eHEA in the cathode and anode confirmed the metallic state and heavily oxidised state, respectively (**Supplementary Figs. S20 and S21**). After the CP test, the alloy's composition remained almost unchanged (except for Nb as Nb₂O₅ at the OER), which indicate that the surface structures are stable after the self-selection, and there was no Ir contaminations from the system (**Supplementary Fig. S22**). For comparison, the cycling stability of 4eHEA and 5eHEA was similarly investigated (**Supplementary Fig. S23**). Pt/C-4eHEA showed no degradation but low performance, whereas Pt/C-5eHEA showed high performance as well as degradation (**Figs. 3a and 3b**). These results indicate that the combination of Ti, Zr, Nb, and Mo (i.e., 4eHEA) yields good passivation performance, while that of Cr, Mn, Fe, Co, and Ni (i.e., 5eHEA) gives good catalytic performance.

Computational study of the catalytic mechanism

To understand the catalytic activities of each element in the HEA and obtain deep insight from the EC-XPS results, we modelled the structures of 9eHEA (**Fig. 4a**) and estimated the Gibbs free energy for HER and OER processes by high-throughput DFT calculations, with the aid of a machine-learning force field (MLFF) generated from DFT-molecular dynamics (MD) simulation. We generated 49 slab models, whose surface areas were around $1.5 \text{ nm} \times 1.5 \text{ nm}$. The computational details and typical adsorption structures are given in **Supplementary Information** and **Supplementary Figs. S24–S28**. In the case of HER^{40,41}, highly efficient catalysts tend to have their Gibbs free energy for H* adsorption, $|\Delta G_{\text{H}^*}|$, close to zero. For example, ΔG_{H^*} for Pt ($\Delta G_{\text{H}^*}^{\text{Pt}}$) is approximately -0.08 eV . ΔG_{H^*} of each element on the 9eHEA surface at 1796 calculation sites can take positive (2.3%) or negative (97.7%) values (**Fig. 4b**). In particular, Mn (range: -0.0088 to -0.097 eV , 7 sites) and Fe (range: -0.0064 to -0.106 eV , 8 sites) could be active sites as effective as Pt. Note that the nearest neighbour elements to the catalytically active sites

with $|\Delta G_{H^*}| < 0.10$ eV are Cr and Fe (15/26 sites) (**Supplementary Table 6**), which means that these elements enhance the catalytic activity of the active sites. Moreover, we calculated the Gibbs free energies of the OER processes^{42,43} at 270 sites, and focused on the $|\Delta G_{O^*}|$ (strong adsorption of O^* intermediate on the catalytic site) under an applied potential of 1.23 V (vs. RHE) as the rate-determining step in the OER processes (**Fig. 3c**). Fe, Co, and Ni showed low adsorption energies of $\Delta G_{O^*} = -2.36$, -1.98 , and -1.00 eV, respectively, in agreement with the experimental findings. Note that for the catalytically active sites in the system with the largest $|\Delta G| < 3.0$ eV, 71% of their nearest neighbour elements are Fe, Mn, or Cr (27/38 sites, **Supplementary Table 7**). Therefore, these three elements promote OER processes on the active sites. The interplay of active sites and their nearest neighbour elements is important for enhancing the catalytic activities for HER and OER. Furthermore, we simulated the OER processes on an initially oxidised surface to reflect the real OER situation by using the model with the segregated Ni suggested by EC-XPS (**Supplementary Fig. S11**). The pre-oxidised surface reduced the activation energy by 0.99 eV (from -2.00 eV to -1.02 eV, **Fig. 3f**). Thus, the oxidation state near catalytically active sites is also crucial for enhancing the OER activity and this finding arises as a consequence of the self-selection/reconstruction (**Scheme 1**).

Discussion

We report a bifunctional electrode catalyst based on HEA (9eHEA) and explored the mechanisms of its high corrosion resistance and high catalytic activity by combining EC-XPS measurements, PEM-type water electrolysis experiments, and DFT calculations of Gibbs free energy profiles. The cooperative 'self-selection' process in 9eHEA creates surface compositions/structures similar to those found in 4eHEA. During the target reactions, the 'self-reconstruction' process causes automatic, cell voltage-dependent segregation and integration of Co and Ni elements, providing favourable conditions for OER. The nine elements in 9eHEA can be classified according to their roles in PEM-type water electrolysis into: HER active elements (Mn, Fe), support elements enhancing HER (Cr and Fe), OER-active elements (Fe, Co, and Ni), support elements enhancing OER (Fe, Mn, and Cr), and passivation elements (Ti, Zr, Nb, and Mo). This classification is supported by further observations of other HEAs containing fewer elements: (i) 5eHEA showed a higher catalytic activity than 4eHEA, (ii) 4eHEA demonstrated no degradation in the target reaction (OER), and (iii) both 4eHEA and 5eHEA showed lower catalytic performances than 9eHEA. Thus, the catalytically active elements (i.e., those in 5eHEA) and the passivation group of elements (i.e., those in 4eHEA) have synergetic effects in 9eHEA to simultaneously achieve high corrosion resistance (**Fig. 2a**) and high catalytic activity (**Fig. 3a and 3b**). Furthermore, we tried to find the best HEA catalyst using the bottom-up approach (**Scheme 1**) by synthesising 5eHEA (Cr, Mn, Fe, Co, and Ni), 6eHEA (Cr, Mn, Fe, Co, Ni, and Mo), 7eHEA (Cr, Mn, Fe, Co, Ni, Nb, and Mo), and 8eHEA (Cr, Mn, Fe, Co, Ni, Zr, Nb, and Mo). By adding one HER- and/or OER-active element at a time, we gradually improved the catalytic performance (**Supplementary Figs. S29–S32**) and finally reached 9eHEA. However, this approach is both cost- and time-consuming compared to the proposed top-down approach.

In conclusion, our systematic study revealed the fundamental mechanism of corrosion-resistant bifunctional electrode catalysts based on HEAs, and provided the proof-of-concept for the top-down approach to optimise HEA catalysts for practical PEM-type electrolyzers. Our findings indicate that the cooperative self-selection of elements and the self-reconstruction of structures on the surface can accelerate the design and computational simulation of multi-element alloys by minimising the costly and lengthy trial-and-error processes. The resultant non-noble metal electrodes with high stability during the applied voltage cycles may be employed in PEM-type electrolyzers driven by renewable power in particular wind power. Due to the scalable (~ 100 kg/time), cost-efficient (300 – 400 dollar/kg) and material processing system such as arc melting and ball milling apparatus, the HEA catalysts can contribute the global usage of PEM-type water electrolysis. More broadly, the corrosion-resistant multi-element alloys with high catalytic activity would be crucial for replacing noble metal catalysts in not only PEM-type water electrolysis but also other types of electrolyzers, electrolytic syntheses, and batteries.

Methods

Preparation of HEA catalysts. Button-like ingots of high-entropic alloy (HEA) were prepared by arc melting in pure Ar atmosphere (99.9999%, 60 kPa). Each alloy ingot (total weight: 20 g) was synthesised from the following mother metals: Ti (99.9 wt%), Cr (99.99 wt%), Mn (99.99 wt%), Fe (99.95 wt%), Co (99.995 wt%), Ni (99.995 wt%), Zr (99.9 wt%), Nb (99.9 wt%), and Mo (99.9 wt%). The mother metals were obtained from Hirano Seizaemon Syouten Co. LTD, Rare Metallic Co. LTD., Japan Metal Service, Furuuchi Chemical Co., and Materials Research Corp. Prior to melting the mother metal ingots, a piece of Ti was melted as a conventional oxygen getter. Equimolar amounts of all nine metals were well-melted, and then additional Mn (10% equimolar amount) was introduced due to Mn's tendency for evaporation (i.e. low boiling point and higher vapour pressure). After complete dissolution of the mother metals, turnover and re-melting of the ingot were repeated at least 6 times to make uniformly mixed alloys (i.e. homogenisation). The other HEAs (4e, 5e, 6e, 7e and 8e HEA) were prepared similarly. The prepared HEA alloy ingot (Fig. 1a) was mixed with carbon black (CB; Aldrich, product number: 05-1530) in 1:1 weight ratio and then milled with ZrO₂ grinding balls in 1:4 weight ratio HEA/CB to ZrO₂ balls (5 mm diameter) at 60 rpm for 6 days. The ball-milled powder was then collected and denoted as HEA/CB.

Sample characterisation. The morphology and microstructure of as-synthesised samples were characterised using scanning electron microscopy (SEM; JEOL JCM-7000 NeoScope), transmission electron microscopy (TEM; JEOL JEM – ARM200F), and the equipped apparatus for energy dispersive spectroscopy (EDS; SDD Type, detection surface area 30 mm², solid angle 0.26 sr). X-ray diffraction (XRD) analysis was carried out using a D2 PHASER (Cu K α 1 radiation; λ = 1.5406 Å, Bruker). X-ray fluorescence (XRF) spectra were measured using EDX-720 (Shimadzu). The surface chemical states were studied with X-ray photoelectron spectroscopy (XPS; AXIS ultra DLD, Shimadzu) with Al K α irradiation and an X-ray monochromator.

Corrosion experiments. Corrosion of the HEAs was measured in a typical three-electrode electrochemical cell at 25°C with an electrochemical workstation (Biologic, VSP-300). An Ag/AgCl electrode saturated with

KCl, a graphite rod, and 0.5 M aqueous H₂SO₄ (pH = 0.5, 95%, Wako, Japan) served as the reference electrode, counter electrode, and electrolyte, respectively. The potential was calculated with respect to reversible hydrogen electrode (RHE) using the equation $E_{\text{RHE}} = E_{\text{Ag/AgCl}} + 0.0591 \times \text{pH} + 0.197$. The working electrode was prepared by dispensing 5.6 μL of a catalytic ink onto a disc of glassy carbon (GC; 5.0 cm diameter), resulting in a catalyst loading of 178 $\mu\text{g}_{\text{HEA}} \text{cm}^{-2}$. To prepare the catalytic ink, 7.0 mg of the crushed 4e, 7e or 9eHEA/CB (in 1:1 weight ratio) and 200 μL of Nafion (5 wt.%, Wako, Japan) were added to 1800 μL of isopropyl alcohol (IPA, 99.7%, Wako, Japan). The ink was homogenised using an ultrasonic bath for 10 min. Before corrosion experiments, N₂ (99.99%) was passed through the electrolyte for at least 30 min to remove any dissolved reactive gases. Then, 50 cyclic voltammetry (CV) cycles were recorded in the potential range between 0.05 and 1.45 V (vs. RHE) at the scan rate of 50.0 mV s^{-1} . Subsequently, an anodic and a cathodic polarisation curves were acquired at the scan rate of 0.10 mV s^{-1} in the respective potential ranges of - 0.55 to 2.2 V (vs. RHE) and 2.2 to - 0.55 V (vs. RHE).

Electrochemical XPS measurements. A piece of 9eHEA with a diameter of approximately 7 mm was cut and mirror-polished with sandpaper and fine alumina slurries (Baikalox, BAIKOWSKI, France). The area of the polished surface was 0.340 cm^2 . After introduction into the UHV system, carbon contamination and oxide layer on the alloy surface were removed by Ar ion etching at 3 keV. A clean, metallic surface on the test alloy was confirmed by XPS (ESCA5800, ULVAC-PHI, Japan) combined with an electrochemical chamber^{20,21}. Electrochemical measurements were performed in 2.5 mM H₂SO₄ electrolyte (pH = 2.3) in the electrochemical chamber filled with high-purity N₂ (G1, 99.99995 vol%, Taiyo Nippon Sanso, Japan). Note that the low concentration of H₂SO₄ minimised residual electrolytes on the electrode surface during the emersion process. After removing all oxides on its surface, HEA was immersed as a working electrode in the electrolyte, with a piece of Pt foil and a reversible hydrogen electrode as the counter and reference electrode, respectively, at open circuit potential (OCP) which corresponds to the corrosion potential of 9eHEA. Linear sweep voltammetry (LSV) was performed with a sweep rate of 2.0 mV s^{-1} from the OCP to a designated electrode potential. The potential was applied for 5 min before the emersion process. After measurement at each potential, the HEA was taken out of the electrolyte solution, the electrochemical chamber was evacuated quickly using a combination of a sorption pump and a cryopump, and the HEA electrode was transferred into the XPS chamber. This emersion process from the electrolyte solution to UHV usually took approximately 5 min without exposing the electrode surface to air. The XPS measurements were performed from - 10 to 1000 eV in the survey scan mode, and then each element was investigated in the narrow scan mode. In addition, the detector was moved from 45° to 75° for depth analysis. After measuring the OER processes, the HEA was mirror-polished again and used to measure the HER processes in similar ways. All spectra were referred to Nb, which showed the most stable intensity. For each element, the chemical species were assigned on the basis of binding energies reported in the ULVAC-PHI database⁴⁴.

Fabrication of MEA. Anode and cathode catalyst inks were prepared. For each MEA sample, ball-milled HEA/CB powder (30 mg), Nafion™ solution (57 μL for the anode ink, 104 μL for the cathode ink), and

IPA/deionised water (1.8 mL:0.2 mL) were sonicated for 1 h to produce a homogeneous ink. A Nafion 115 membrane (thickness: 125 μm , active area: 4.0 cm^2) was treated by sequential immersion to remove contaminations on the membrane in (i) 3.0 wt% H_2O_2 solution at 80°C for 1 h, (ii) deionised water (18.2 M Ω cm, Millipore) at 80°C for 1 h, (iii) 1.0 M H_2SO_4 solution at 80°C for 1 h, and (iv) deionised water at 80°C for another 1 h. The prepared catalyst ink was then spray-deposited onto the pre-heated (120°C) Nafion membrane using an Aerograph airbrush to form a catalyst layer, with a loading amount of 6.0 mg cm^{-2} for HEA/CB and 1.0 mg cm^{-2} for Pt/C or IrO_2 . Note that HEA catalyst inks without CB were not dispersed well in the IPA/deionized water and then the spray-deposition was failed. Subsequently, a gas diffusion layer (GDL) made of mesoporous carbon paper (SGL Carbon, GDL 22BB) surface-coated with CB was hot-pressed onto the cathode catalyst layer on a pre-heated hot-press (130°C) at 5.0 MPa (50 kg cm^{-2}) for 3 min. An MEA consisting of the noble metal catalysts Pt/C and IrO_2 (loading amount: 1.0 mg cm^{-2} for each) was similarly prepared as benchmarks.

PEM-type water electrolysis test. A potentiostat (VSP-300, Biologic) equipped with booster units (30 A) was used to carry out the single-cell experiments, which all used a cell temperature of 80°C and ambient pressure. Deionised water at 85°C was supplied to the anode side at a flow rate of 10 mL min^{-1} . The cell was conditioned by ramping the current density to 5.0 A cm^{-2} and then holding it for at least 2 h before the tests to remove easy-to-dissolve metals and other contaminations. Stable I - V polarisation curves were recorded from 0 to 5.0 A cm^{-2} at a scan rate of 5.0 mV s^{-1} . Accelerated stress tests were performed by scanning the cell voltage between 0 and 3.2 V with a scan rate of 1.0 V s^{-1} for 1000 cycles. In CV experiments, the cell voltage in the cyclic voltammogram was automatically iR -compensated with the Ohmic resistance measured at 0.0 V (vs. RHE). Chronopotentiometry (CP) was performed by holding the current density at 1.0 A cm^{-2} and recording the data for 100 h. Electrochemical impedance spectroscopy (EIS) measurements were performed in the frequency range of 100 MHz–20 kHz with current perturbations of ± 200 mA at cell voltages ranging from 1.6 to 2.7 V.

DFT calculations. DFT calculations were performed with the VASP code⁴⁵ using the projected augmented wave (PAW) method⁴⁶. The Perdew-Burke-Ernzerhof (PBE) functional⁴⁷ was employed as the exchange-correlation functional. The plane wave energy cutoff was set to 400 Ry. Because the atomic-level structure of 9eHEA was not known, we adopted a high-throughput protocol with the aid of machine learning. First, a cubic cell (edge length: 15 Å) was created, and 216 atoms (24 atoms per species) were inserted into it. After 5 ps of equilibration, we ran 30 ps of DFT-MD simulation with the time step of 2 fs. DFT-MD simulation was performed at 3000 K in the NVT ensemble. Such a high temperature was adopted to avoid the structure being trapped in local minima and to accelerate the configurational sampling. However, 30 ps was too short for unbiased sampling of 9eHEA structures, and therefore a MLFF was constructed from the DFT-MD trajectory based on the Gaussian approximated potential (GAP)⁴⁸ and smooth overlap of atomic potential (SOAP)⁴⁹ schemes. Using the constructed MLFF, we ran 10 ns of classical MD simulations at 3000 K using the LAMMPS package⁵⁰ and picked 7 snapshots. Starting from these snapshots, we further ran 5 ps of DFT-MD simulation and then optimised the bulk

structures including the unit cell vectors. Seven surface slab models were created from each bulk structure by inserting vacuum at $z = 0, 2, 4, 6, 8, 10,$ and 12 \AA . In this way, we obtained 7 (bulk structures) $\times 7$ (surfaces) $\times 2$ (up and down sides of the slab model) = 98 surface models of 9eHEA. After optimising the slab model, we added the intermediate species for HER and OER on the surface atoms, and calculated energy diagrams according to the protocol described in Supplementary Information.

Declarations

Data Availability

The data that support the findings of this study are available from the corresponding authors upon reasonable request.

Supplementary information is available for this paper at XXX.

References

1. Haryanto, A., Fernando, S., Murali, N. & Adhikari, S. Current status of hydrogen production techniques by steam reforming of ethanol: A review. *Energy Fuels* 19, 2098–2106 (2005). 10.1021/ef0500538.
2. Tang, C., Zheng, Y., Jaroniec, M. & Qiao, S. Z. Electrocatalytic Refinery for Sustainable Production of Fuels and Chemicals. *Angew. Chem. Int. Ed.* 60, 19572–19590 (2021). 10.1002/anie.202101522.
3. Hubert, M. A., King, L. A. & Jaramillo, T. F. Evaluating the Case for Reduced Precious Metal Catalysts in Proton Exchange Membrane Electrolyzers. *ACS Energy Lett.* 7, 17–23 (2022). 10.1021/acscenergylett.1c01869.
4. Zeng, K. & Zhang, D. Recent progress in alkaline water electrolysis for hydrogen production and applications. *Prog. Energy Combust. Sci.* 36, 307–326 (2010). 10.1016/j.pecs.2009.11.002.
5. Mo, J., Kang, Z., Retterer, S. T., Cullen, D. A., Toops, T. J., Green, J. B. Jr., Mench, M. M. & Zhang, F.Y. Discovery of true electrochemical reactions for ultrahigh catalyst mass activity in water splitting. *Sci. Adv.* 2, e1600690 (2016). 10.1126/sciadv.1600690.
6. Carmo, M., Fritz, D. L., Mergel, J. & Stolten, D. A comprehensive review on PEM water electrolysis. *Int. J. Hydrog. Energy.* 38, 4901–4934 (2013). 10.1016/j.ijhydene.2013.01.151.
7. Li, D., Park, E. J., Zhu, W., Shi, Q., Zhou, Y., Tian, H., Lin, Y., Serov, A., Zulevi, B., Baca, E. D., Fujimoto, C., Chung, H. T. & Kim, Yu. S. Highly quaternized polystyrene ionomers for high performance anion exchange membrane water electrolyzers. *Nat. Energy* 5, 378–385 (2020). 10.1038/s41560-020-0577-x.
8. Xu, D., Stevens, M. B., Cosby, M. R., Oener, S. Z., Smith, A. M., Enman, L. J., Ayers, K. E., Capuano, C. B., Renner, J. N., Danilovic, N., Li, Y., Wang, H., Zhang, Q. & Boettcher, S. W. Earth-abundant oxygen electrocatalysts for alkaline anion-exchange-membrane water electrolysis: Effects of catalyst

- conductivity and comparison with performance in three-electrode cells. *ACS Catal.* 9, 7–15 (2019). 10.1021/acscatal.8b04001.
9. Miller, H.A., Bouzek, K., Hnat, J., Loos, S., Bernäcker, C.I., Weißgärber, T., Röntzsch, L., & Meier-Haack, J. Green hydrogen from anion exchange membrane water electrolysis: a review of recent developments in critical materials and operating conditions. *Sustain. Energ. Fuels* 4, 2114–2133 (2020). 10.1039/C9SE01240K.
 10. Abbasi, R., Setzler, B. P., Lin, S., Wang, J., Zhao, Y., Xu, H., Pivovar, B., Tian, B., Chen, X., Wu, G. & Yan, Y. A road map to low-cost hydrogen with hydroxide exchange membrane electrolyzers, *Adv. Mater.* Mater 31, 1905876 (2019). 10.1002/adma.201805876.
 11. Global hydrogen Review 2021. <https://www.iea.org/reports/global-hydrogen-review-2021> (Int. Energy Agency).
 12. Dodwell, J., Maier, M., Majasan, J., Jervis, R., Castanheira, L., Shearing, P., Hinds, G. & Brett, D.J.L. Open-circuit dissolution of platinum from the cathode in polymer electrolyte membrane water electrolyzers. *J. Power Sources* 498, 229937 (2021). 10.1016/j.jpowsour.2021.229937.
 13. Knöppel, J., Möckl, M., López, D. E., Stojanovski, K., Bierling, M., Böhm, T., Thiele, S., Rzepka, M., & Cherevko, S. On the limitations in assessing stability of oxygen evolution catalysts using aqueous model electrochemical cells. *Nat. Commun* 12, 2231 (2021). 10.1038/s41467-021-22296-9.
 14. Chen, Z. J., Zhang, T., Gao, X. Y., Huang, Y. J., Qin, X. H., Wang, Y. F., Zhao, K., Peng, X., Zhang, C., Liu, L., Zeng, M. H. & Yu, H. B. Engineering microdomains of oxides in high-entropy alloy electrodes toward efficient oxygen evolution. *Adv. Mater.* 33, 2101845 (2021). 10.1002/adma.202101845
 15. Zhang, L., Cai, W. & Bao, N. Top-level design strategy to construct an advanced high-entropy Co-Cu-Fe-Mo (oxy)hydroxide electrocatalyst for the oxygen evolution reaction. *Adv. Mater.* 33, 2100745 (2021). 10.1002/adma.202100745.
 16. McKay, F., Fang, Y., Kizilkaya, O., Singh, P., Johnson, D. D., Roy, A., Young, D. P., Sprunger, P. T., Flake, J. C., Shelton, W. A. & Xu, Y. CoCrFeNi high-entropy alloy as an enhanced hydrogen evolution catalyst in an acidic solution. *J. Phys. Chem. C Nanomater. Interfaces* 125, 17008–17018 (2021). 10.1021/acs.jpcc.1c03646.
 17. Zhang, Y., Dai, W., Zhang, P., Lu, T. & Pan, Y. In-situ electrochemical tuning of $(\text{CoNiMnZnFe})_3\text{O}_{3.2}$ high-entropy oxide for efficient oxygen evolution reactions. *J. Alloys Compd* 868, 159064 (2021). 10.1016/j.jallcom.2021.159064.
 18. Feng, D., Dong, Y., Nie, P., Zhang, L. & Qiao, Z.-A. CoNiCuMgZn high entropy alloy nanoparticles embedded onto graphene sheets via anchoring and alloying strategy as efficient electrocatalysts for hydrogen evolution reaction. *Chem. Eng. J.* 430, 132883 (2022). 10.1016/j.cej.2021.132883.
 19. Huang, K., Peng, D., Yao, Z., Xia, J., Zhang, B., Liu, H., Chen, Z., Wu, F., Wu, J. & Huang, Y. Cathodic plasma driven self-assembly of HEAs dendrites by pure single FCC FeCoNiMnCu nanoparticles as high efficient electrocatalysts for OER. *Chem. Eng. J.* 425, 131533 (2021). 10.1016/j.cej.2021.131533.

20. Qiu, H.-J., Fang, G., Gao, J., Wen, Y., Lv, J., Li, H., Xie, G., Liu, X. & Sun, S. Noble metal-free nanoporous high-entropy alloys as highly efficient electrocatalysts for oxygen evolution reaction. *ACS Mater. Lett.* 1, 526–533 (2019). 10.1021/acsmaterialslett.9b00414.
21. Ding, Z., Bian, J., Shuang, S., Liu, X., Hu, Y., Sun, C. & Yang, Y. High entropy intermetallic–oxide core–shell nanostructure as superb oxygen evolution reaction catalyst. *Adv. Sustain. Syst.* 4, 1900105 (2020). 10.1002/adsu.201900105.
22. Zhang, G., Ming, K., Kang, J., Huang, Q., Zhang, Z., Zheng, X. & Bi, X. High entropy alloy as a highly active and stable electrocatalyst for hydrogen evolution reaction. *Electrochim. Acta* 279, 19–23 (2018). 10.1016/j.electacta.2018.05.035.
23. Qiu, Y., Thomas, S., Gibson, M. A., Fraser, H. L. & Birbilis, N. Corrosion of high entropy alloys. *NPJ Mater. Degrad.* 1, 15 (2017). 10.1038/s41529-017-0009-y.
24. Wakisaka, M., Udagawa, Y., Suzuki, H., Uchida, H. & Watanabe, M. Structural effects on the surface oxidation processes at Pt single-crystal electrodes studied by X-ray photoelectron spectroscopy. *Energy Environ. Sci.* 4, 1662–1666 (2011). 10.1039/c0ee00756k.
25. Wakisaka, M., Mitsui, S., Hirose, Y., Kawashima, K., Uchida, H. & Watanabe, M. Electronic structures of Pt – Co and Pt – Ru alloys for CO-tolerant anode catalysts in polymer electrolyte fuel cells studied by EC – XPS. *J. Phys. Chem. B* 110, 23489–23496 (2006). 10.1021/jp0653510.
26. Barrett, E. P., Joyner, L. G. & Halenda, P. P. The determination of pore volume and area distributions in porous substances. I. Computations from nitrogen isotherms. *J. Am. Chem. Soc.* 73, 373–380 (1951). 10.1021/ja01145a126.
27. McCafferty, E. Validation of corrosion rates measured by the Tafel extrapolation method. *Corros. Sci.* 47, 3202–3215 (2005). 10.1016/j.corsci.2005.05.046.
28. Quartarone, G., Bellomi, T. & Zingales, A. Inhibition of copper corrosion by isatin in aerated 0.5 M H₂SO₄. *Corros. Sci.* 45, 715–733 (2003). 10.1016/S0010-938X(02)00134-8.
29. Tahmasebi, S., Hossain, M. A. & Jerkiewicz, G. Corrosion behavior of platinum in aqueous H₂SO₄ solution: Part 1 - Influence of the potential scan rate and the dissolved gas. *Electrocatalysis* 9, 172–181 (2018). 10.1007/s12678-018-0454-6.
30. Tahmasebi, S., Jerkiewicz, G., Baranton, S., Coutanceau, C., Furuya, Y. & Ohma, A. How Stable Are Spherical Platinum Nanoparticles Applied to Fuel Cells? *J. Phys. Chem. C* 122, 11765–11776 (2018). 10.1021/acs.jpcc.7b10617.
31. Tahmasebi, S., Jahangiri, S., Mosey, N., Jerkiewicz, G., Baranton, S., Coutanceau, C., Furuya, Y. & Ohma, A. Oxidation and Corrosion of Platinum–Nickel and Platinum–Cobalt Nanoparticles in an Aqueous Acidic Medium. *ACS Appl. Energy Mater.* 2, 7019–7035 (2019). 10.1021/acsaem.9b00625.
32. Lu, G. & Zangari, G. Corrosion resistance of ternary NiP based alloys in sulfuric acid solutions. *Electrochim. Acta* 47, 2969–2979 (2002). 10.1016/S0013-4686(02)00198-6.
33. Lorenz, W. J. & Mansfeld, F. Determination of corrosion rates by electrochemical DC and AC methods. *Corros. Sci.* 21, 647–672 (1981). 10.1016/0010-938X(81)90015-9.

34. Kao, Y.-F., Lee, T.-D., Chen, S.-K. & Yee-Shyi, C. Electrochemical passive properties of $\text{Al}_x\text{CoCrFeNi}$ ($x = 0, 0.25, 0.50, 1.00$) alloys in sulfuric acids. *Corros. Sci.* 52 1026–1034 (2010). 10.1016/j.corsci.2009.11.028.
35. Chou, Y. L., Yeh, J. W. & Shih, H. C. The effect of molybdenum on the corrosion behaviour of the high-entropy alloys $\text{Co}_{1.5}\text{CrFeNi}_{1.5}\text{Ti}_{0.5}\text{Mo}_x$ in aqueous environments. *Corros. Sci.* 52, 2571–2581 (2010). 10.1016/j.corsci.2010.04.004.
36. Lee, C. P., Chang, C. C., Chen, Y. Y., Yeh, J. W. & Shih, H. C. Effect of the aluminium content of $\text{Al}_x\text{CrFe}_{1.5}\text{MnNi}_{0.5}$ high-entropy alloys on the corrosion behaviour in aqueous environments. *Corros. Sci.* 50, 2053–2060 (2008). 10.1016/j.corsci.2008.04.011.
37. Tait, W. S. *An Introduction to* (Electrochemical Corrosion Testing for Practicing Engineers and Scientists, Racine, WI, 1994).
38. Conway, B. E. Electrochemical oxide film formation at noble metals as a surface-chemical process. *Prog. Surf. Sci.* 49, 331–452 (1995). 10.1016/0079-6816(95)00040 – 6.
39. Wakisaka, M., Asizawa, S., Uchida, H. & Watanabe, M. In situ STM observation of morphological changes of the Pt(111) electrode surface during potential cycling in 10 mM HF solution. *Phys. Chem. Chem. Phys.* 12, 4184–4190 (2010). 10.1039/b923956a.
40. Nørskov, J. K., Bligaard, T., Rossmeisl, J. & Christensen, C. H. Towards the computational design of solid catalysts. *Nat. Chem.* 1, 37–46 (2009). 10.1038/nchem.121.
41. Greeley, J., Jaramillo, T. F., Bonde, J., Chorkendorff, I. B. & Nørskov, J. K. Computational high-throughput screening of electrocatalytic materials for hydrogen evolution. *Nat. Mater.* 5, 909–913 (2006). 10.1038/nmat1752.
42. Friebel, D., Louie, M. W., Bajdich, M., Sanwald, K. E., Cai, Y., Wise, A. M., Cheng, M. J., Sokaras, D., Weng, T. C., Alonso-Mori, R., Davis, R. C., Bargar, J. R., Nørskov, J. K., Nilsson, A. & Bell, A. T. Identification of highly active Fe sites in (Ni,Fe)OOH for electrocatalytic water splitting. *J. Am. Chem. Soc.* 137, 1305–1313 (2015). 10.1021/ja511559d.
43. Doyle, R. L., Godwin, I. J., Brandon, M. P. & Lyons, M. E. G. Redox and electrochemical water splitting catalytic properties of hydrated metal oxide modified electrodes. *Phys. Chem. Chem. Phys.* 15, 13737–13783 (2013). 10.1039/c3cp51213d.
44. Moulder, J. F., Stickle, W. F., Sobol, P. E. & Bomben, K. D. *Handbook of X-Ray Photoelectron Spectroscopy* (ed. Chastain, J. & King, R. C.) (Physical Electronics, Inc., USA, 1995).
45. Kresse, G. & Hafner, J. Norm-conserving and ultrasoft pseudopotentials for first-row and transition elements. *J. Phys.: Condens. Matter* 6, 8245–8257 (1994). 10.1088/0953–8984/6/40/015.
46. Blöchl, P. E. Projector augmented-wave method. *Phys. Rev. B Condens. Matter* 50, 17953–17979 (1994). 10.1103/physrevb.50.17953.
47. Perdew, J. P., Burke, K. & Ernzerhof, M. Generalized gradient approximation made simple. *Phys. Rev. Lett.* 77, 3865–3868 (1996). 10.1103/PhysRevLett.77.3865.

48. Bartók, A. P., Payne, M. C., Kondor, R. & Csányi, G. Gaussian approximation potentials: The accuracy of quantum mechanics, without the electrons. *Phys. Rev. Lett.* 104, 136403 (2010). 10.1103/PhysRevLett.104.136403.
49. Bartók, A. P., Kondor, R., & Csányi, G. On representing chemical environments. *Phys. Rev. B* 87, 184115 (2013). 10.1103/PhysRevB.96.019902.
50. Thompson, A. P., Aktulga, H. M., Berger, R., Bolintineanu, D. S., Brown, W. M., Crozier, P. S., in't Veld, P. J., Kohlmeyer, A., Moore, S. G., Nguyen, T. D. & Shan, R. LAMMPS - a flexible simulation tool for particle-based materials modeling at the atomic, meso, and continuum scales. *Comp. Phys. Commun.* 271, 108171 (2022). 10.1016/j.cpc.2021.108171.

Schemes

Scheme 1 is in the supplementary files section.

Figures

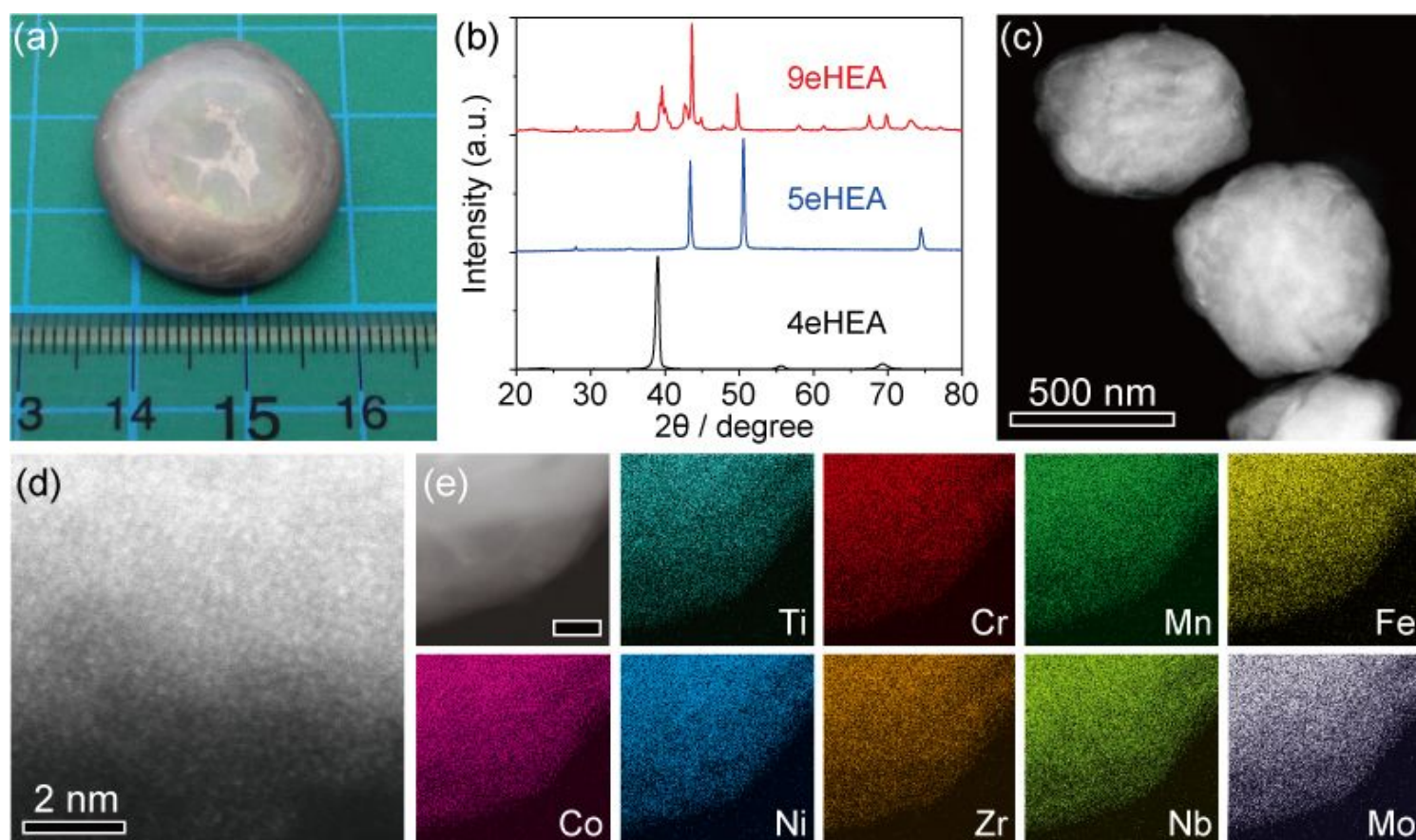


Figure 1

Characterisations of HEAs. (a) Photograph of 9eHEA ingot. (b) XRD patterns of HEAs. DF-STEM images of 9eHEA at (c) low magnification and (d) high magnification. (e) Elemental maps of the nine elements in 9eHEA, demonstrating the homogeneous distribution of each element. Scale bar in (e): 30 nm.

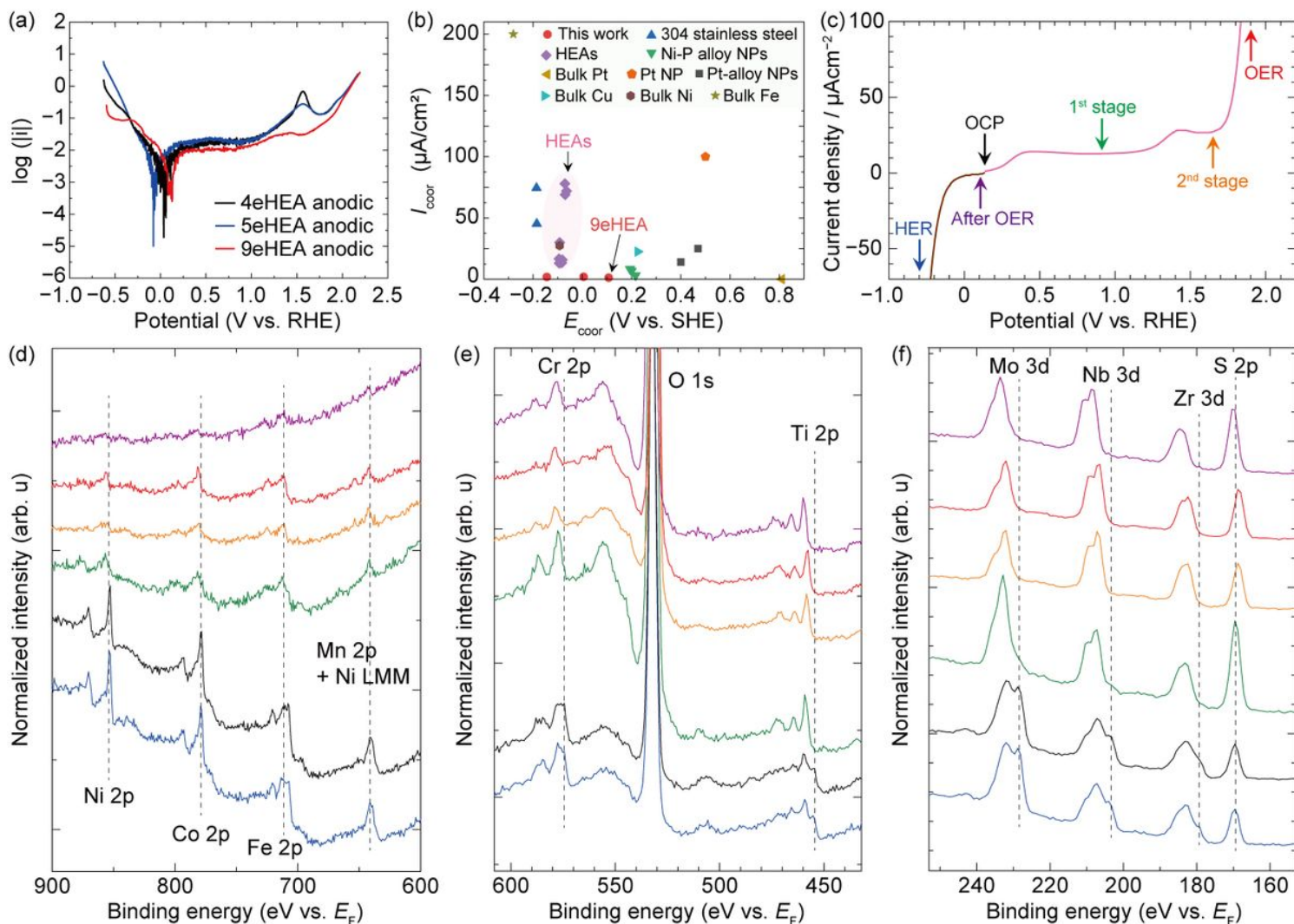


Figure 2

Corrosion-resistant characteristics and self-selection of elements in target reactions. (a) Typical corrosion test of HEAs along the anodic scan direction in 0.5 M H₂SO₄ electrolyte. (b) Corrosion parameters of various metals and alloys. (c) Linear sweep voltammogram of 9eHEA in 2.5 mM H₂SO₄ electrolyte. EC-XPS measurements were performed at the potentials of OCP (0.14 V, black), 1st stage (0.92 V, green), 2nd stage (1.65 V, orange), OER (1.90 V, red), and then after OER (0.07 V, purple) and HER (-0.30 V, blue). (d–f) EC-XPS data in the survey mode for 9eHEA at the potentials indicated in (c) using the same colour codes.

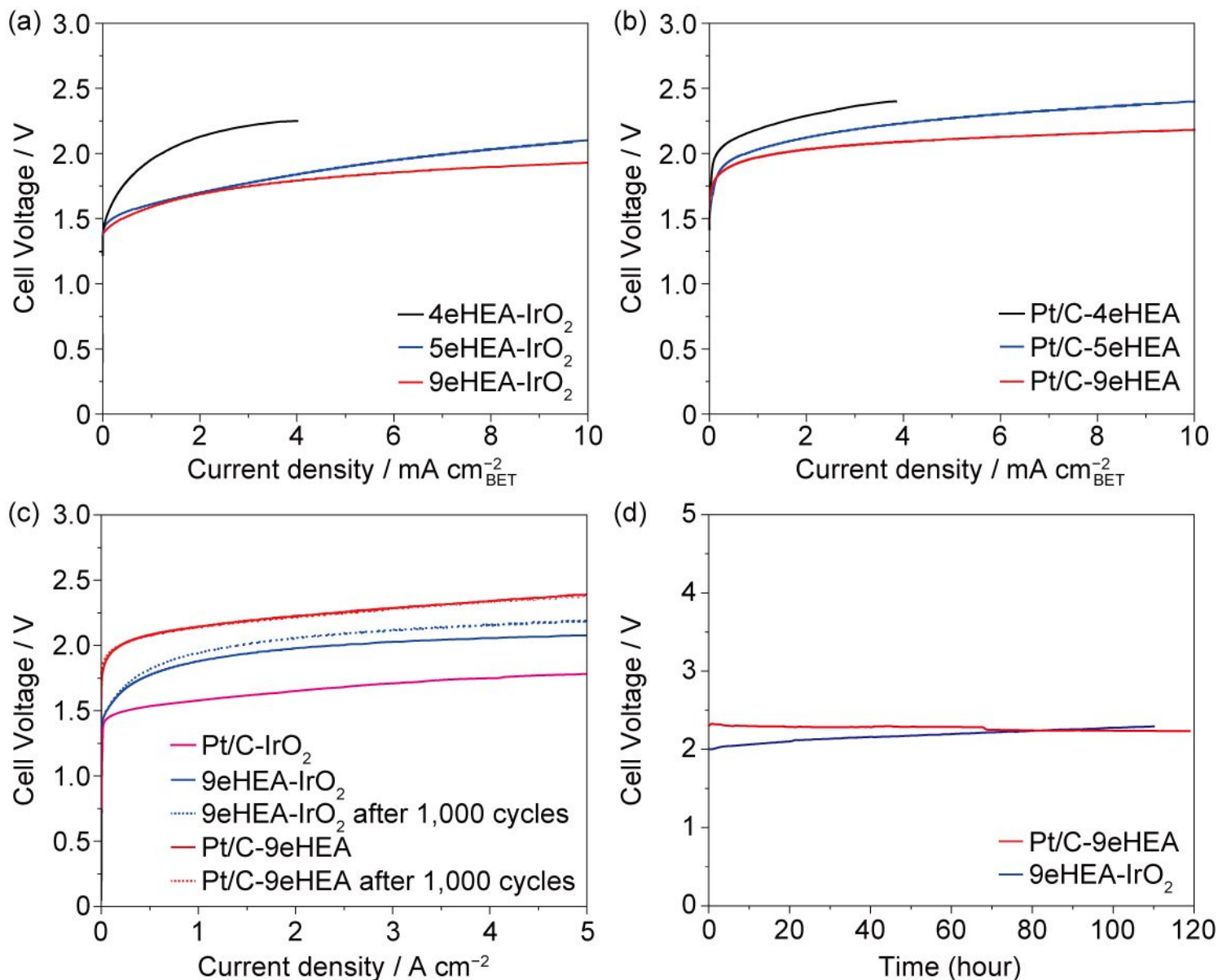


Figure 3

Performance of PEM-type water electrolysis at 80 °C. I - V curves of 4eHEA, 5eHEA, and 9eHEA used in the (a) cathode and (b) anode. The current density is normalised by the total surface area of HEA. (c) Comparison of CV curves in the 1st and 1000th cycles for 9eHEA cathode and anode for cycling stability. The current density is normalised by the electrode surface area (4.0 cm^2). (d) Chronopotentiometry data (iR-included) of 9eHEA cathode and anode at 1.0 A cm^{-2} .

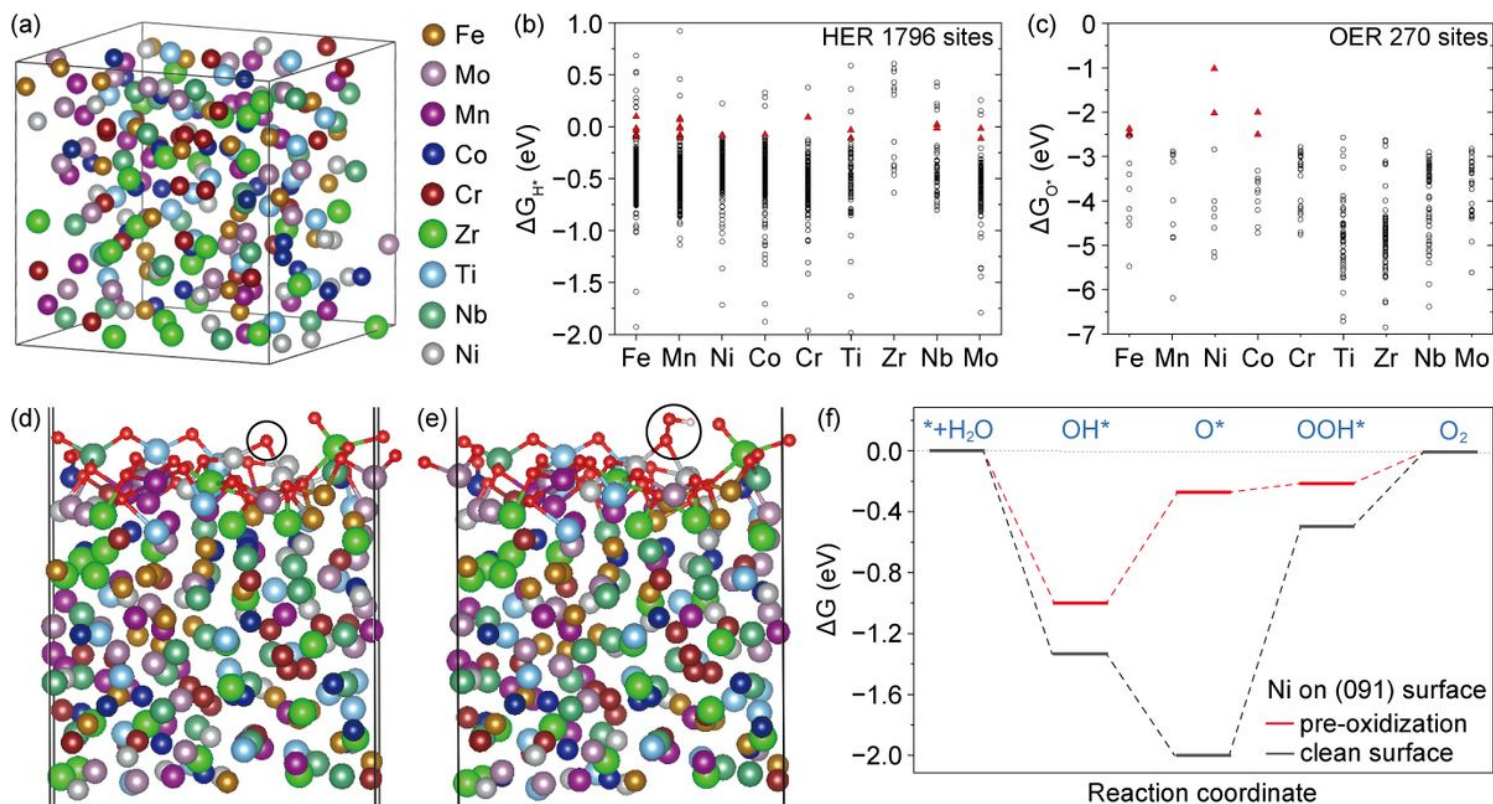


Figure 4

DFT calculation of catalytically active sites on 9eHEA. (a) Calculation model of 9eHEA without oxidation. The Gibbs free energies of (b) HER and (c) OER. Red triangles represent their catalytically active sites. The calculation model of 9eHEA with pre-oxidation for (d) O^* intermediate and (e) OOH^* intermediate. Black circles indicate the intermediates on catalytically active sites (Ni). Red and white balls represent O and H atoms, respectively. (f) Gibbs free energy profiles on the Ni with and without oxidation under an applied potential of 1.23 V.

Supplementary Files

This is a list of supplementary files associated with this preprint. Click to download.

- [SupplementaryinformationDOUBLEBLIND.pdf](#)
- [floatimage1.jpeg](#)